GEOPHYSICS, VOL. 76, NO. 6 (NOVEMBER-DECEMBER 2011); P. C65–C79, 19 FIGS.
10.1190/GEO2010-0079.1

Long-offset AVO inversion of PP reflections from plane interfaces using effective reflection coefficients

Lyubov Skopintseva[1], Milana Ayzenberg[2], Martin Landrø[1], Tatyana Nefedkina[3], and Arkady M. Aizenberg[3]

ABSTRACT

A conventional amplitude variation with offset (AVO) inversion is based on geometrical seismics which exploit plane-wave reflection coefficients to describe the reflection phenomenon. Widely exploited linearizations of plane-wave coefficients are mostly valid at pre-critical offsets for media with almost flat and weak-contrast interfaces. Existing linearizations do not account for the seismic frequency range by ignoring the frequency content of the wavelet, which is a strong assumption. Plane-wave reflection coefficients do not fully describe the reflection of seismic waves at near-critical and post-critical offsets, because reflected seismic waves are typically generated by point sources. We propose an improved approach to AVO inversion, which is based on effective reflection coefficients (ERCs). ERCs generalize plane-wave coefficients for seismic waves generated by point sources and therefore more accurately describe near-critical and post-critical reflections where head waves are generated. Moreover, they are frequency-dependent and incorporate the local curvatures of the wavefront and the reflecting interface. In our study, we neglect the effect of interface curvature and demonstrate the advantages of our approach on synthetic data for a simple model with a plane interface separating two isotropic half-spaces. A comparison of the inversion results obtained with our approach and the results from an AVO inversion method based on the exact plane-wave reflection coefficient suggests that our method is superior, in particular for long-offset ranges which extend to and beyond the critical angle. We thus propose that long offsets can be successfully exploited in an AVO inversion under the correct assumption about the reflection coefficient. Such long-offset AVO inversion shows the potential of outperforming a conventional moderate-offset AVO inversion in the accuracy of estimated model parameters.

INTRODUCTION

Amplitude variation with offset (AVO) inversion converts the measured amplitude of a reflected event into physical medium parameters. The ultimate goal of a deterministic AVO inversion is to estimate the medium parameters through minimization of the misfit between the AVO data extracted from the target reflection and its theoretical description. A successful AVO inversion captures most of the phenomena contained in the observed wavefield.

A reflected event at the receiver can generally be described by the product of a propagation operator through the overburden and a reflectivity function at the target interface. The propagation operator includes the respective phenomena that occur during wave propagation, such as energy flux along ray tubes, focusing, attenuation, transmission losses, diffraction, etc. The propagation effects are usually compensated for through dedicated preprocessing of the AVO data.

The reflectivity function widely exploited in conventional AVO inversion is based on linearizations of the plane-wave reflection coefficient (PWRC) given by the Zoeppritz equations (Aki and Richards, 2002; Shuey, 1985). An underlying assumption is that the contrast in the seismic parameters across the reflecting interface is weak and the incidence angle is small. This limits the applicability of an AVO inversion to pre-critical offsets. The growing industry interest in reservoirs with strong-contrast interfaces (salt domes, heavy oil fields, basalts, etc.) and increased offset ranges in seismic

Manuscript received by the Editor 4 March 2010; revised manuscript received 1 July 2011; published online 27 December 2011.
[1]Norwegian University of Science and Technology, Department of Petroleum Engineering and Applied Geophysics, Trondheim, Norway.
[2]Statoil ASA, Bergen, Norway.
[3]Institute of Petroleum Geology and Geophysics SB RAS, Novosibirsk, Russia.

acquisition led to increased interest in near-critical and post-critical reflections in the data. These are associated with rapid amplitude variations and cannot be described by the linearized plane-wave reflection coefficients. Conventional approaches to AVO inversion cannot be applied in such circumstances. However, there is a potential for enhancing the accuracy of AVO inversion by incorporating and exploiting the near-critical and post-critical offsets.

Riedel and Theilen (2001) and Downton and Ursenbach (2006) were among the first authors to realize the power of long-offset AVO inversion. They exploited the exact Zoeppritz equations to describe the AVO data and showed that they are inadequate at long offsets. The main reason is that the respective equations honor the plane incident waves, when the original AVO data is caused by the nonplane waves and contains head waves.

van der Baan and Smit (2006) suggested to exploit the $\tau - p$ transform to reduce the original AVO data to the plane-wave domain, where the constituting plane waves can be correctly described by PWRCs for small incidence angles. Although this has proven to enhance the quality of AVO inversion, the approach is limited to near-critical offsets and is prone to data sampling issues.

Because a typical seismic source emits a wave which is almost spherical and has finite frequency band, a qualitative and quantitative improvement in AVO inversion can be achieved by incorporating the Fresnel volume, which surrounds the reflected ray (Favretto-Cristini et al., 2009). This will automatically include the seismic frequency range and capture the effect of transversal energy diffusion. It is also natural to expect that the Fresnel zone surrounding the reflection point has an equally strong impact on the reflection strength as the reflection point itself. Červený (1961) and Brekhovskikh (1960) derived reflection coefficients that incorporate the Fresnel zone and are valid for point sources and finite frequencies. Later, Ursenbach et al. (2007) proposed the so-called spherical-wave reflection coefficients which depend on the wavelet form and are valid only for homogeneous media, plane reflectors, and spherical waves.

To generally describe the reflection of arbitrary waves at curved reflectors in inhomogeneous media, De Santo (1983) and Kennett (1984) suggested the implicit local reflection and transmission operators as numerical solutions for acoustic and elastic media. Klem-Musatov et al. (2004) suggested a general rigorous reflection-transmission theory for scalar waves at curved interfaces between heterogeneous media. Later, Aizenberg et al. (2005) extended the theory for acoustic waves. Based on their results, Ayzenberg et al. (2007) and Ayzenberg et al. (2009) developed an explicit approximate description of the reflection at curved interfaces in the form of ERCs for acoustic and elastic waves.

Similarly to the spherical-wave reflection coefficients, ERCs incorporate reflections from the interface points located inside the Fresnel zone. ERCs relax the assumptions of plane wavefront and locally plane reflecting interface implicit in PWRCs. ERCs thus generalize PWRCs and the spherical-wave reflection coefficients for curved reflectors, and are adequate within the seismic frequency range. They capture the associated phenomena at the near-critical and post-critical offsets. Moreover, they do not depend on the wavelet form, unlike the spherical-wave reflection coefficients.

In this paper, we introduce the background theory for the new approach to long-offset AVO inversion based on ERCs. We test the approach on synthetic data for a simple model, where two homogeneous elastic half-spaces are separated by a horizontal plane interface. We propose to exploit two ways of extracting the amplitudes from the data, which we refer to as the single-frequency and the band-limited AVO data, and introduce their respective theoretical descriptions. We perform AVO inversion for different offset ranges, and assess the performance of our approach at long offsets. By comparing the results of our AVO inversion with the results obtained from AVO inversion based on exact PWRCs, we demonstrate the superiority of our inversion with increasing offset range.

The paper is divided in three parts. Part 1 introduces the statement of the AVO inversion problem for long-offset data. We review ERCs and discuss their properties in detail. Part 2 is devoted to the new approach to AVO inversion based on ERCs. We study the impact of the frequency content on AVO inversion. We then proceed to comparing the ERC-based and the PWRC-based AVO inversions. Part 3 demonstrates the advantages of performing a long-offset AVO inversion on a synthetic PP data set for various offset ranges. In the Discussion, we cover some aspects connected with the possibility to exploit ERC-based AVO inversion in practice. In Appendix A, we derive an approximation of the PP reflected wavefield at a receiver in terms of the ERC.

DETERMINISTIC AVO INVERSION

We consider a deterministic AVO inversion approach which consists of updating the model parameters through the minimization of the misfit function between the observed AVO data and its theoretical description:

$$F(\mathbf{v}) = \sqrt{\sum_{n=1}^{N} [AVO_{\text{obs}}(\mathbf{x}_n) - AVO_{\text{theo}}(\mathbf{x}_n)]^2} \rightarrow \min, \quad (1)$$

where $AVO_{\text{obs}}(\mathbf{x}_n)$ is the observed AVO data, $AVO_{\text{theo}}(\mathbf{x}_n)$ represents the theoretical description of the observed AVO data, $\mathbf{v}$ is the vector of required parameters, $\mathbf{x}_n (n = 1, 2, \ldots, N)$ are the receiver coordinates, and N denotes the number of receivers. The dimension of vector $\mathbf{v}$ is equal to the number of unknown parameters.

Extraction of the AVO data by picking the amplitude maximum fails at long offsets because of the phase rotation which occurs at the near-critical and post-critical offsets (Riedel and Theilen, 2001). Lavaud et al. (1999) showed that taking the rms value of the reflected event in the fixed time window along the moveout is appropriate to long-offset data because it is insensitive to the phase changes.

Figure 1 shows the AVO data extracted from a 3D synthetic data set computed using reflectivity modeling (Kennett, 1983). The theoretical plane-wave description of this data is defined by

$$AVO_{\text{theo}}(\mathbf{x}_n) = \frac{|R_{PP}(\theta(\mathbf{x}_n), \mathbf{m})|}{\frac{1}{N}\sum_{n=1}^{N} |R_{PP}(\theta(\mathbf{x}_n), \mathbf{m})|}, \quad (2)$$

where $R_{PP}(\theta(\mathbf{x}_n), \mathbf{m})$ is the exact PWRC, $\mathbf{x}_n$ is the receiver coordinate, $\theta(\mathbf{x}_n)$ is the reflection angle, $\mathbf{m} = (\frac{\rho_2}{\rho_1}, \frac{V_{P2}}{V_{P1}}, \frac{V_{S1}}{V_{P1}}, \frac{V_{S2}}{V_{P2}})$ is a dimensionless parameter vector, as introduced by Petrashen (1957), Lavaud et al. (1999), and Kurt (2007), ρ_1 and ρ_2 are the densities above and below the reflecting interface, V_{P1} and V_{P2} are the P-wave velocities, and V_{S1} and V_{S2} are the S-wave velocities. We observe a good match between the AVO data and the theoretical description only at the pre-critical offsets. The deviation of the plane-wave theoretical description from the AVO data becomes substantial at the near-critical and post-critical offsets. This is explained

by the sphericity of the wavefront and the interference of the reflected and head waves near and beyond the critical incidence angle. The dependence of the theoretical plane-wave description in equation 2 on four dimensionless parameters allows unique recovery of a maximum of four parameters, as stated by the Buckingham pi-theorem (Bluman and Kumei, 1989).

A successful AVO inversion implies an adequate theoretical description of the phenomena contained in the AVO data. One way is to apply the $\tau - p$ transform to the data and exploit AVO inversion based on PWRCs (van der Baan and Smit, 2006). Another way is to account for nonplanar wavefronts by exploiting other reflection coefficients than PWRCs. ERCs represent an alternative to PWRCs for waves generated by point sources (Ayzenberg et al., 2007, 2009).

Although ERCs are valid for curved interfaces and inhomogeneous media, we leave the general ERCs outside the scope of this paper and consider only the particular case of plane interfaces. For a particular case of spherical incident waves, plane reflectors and homogeneous media, ERCs are similar to the spherical-wave reflection coefficients introduced by Ursenbach et al. (2007). The difference is that the former are defined at the interface and the latter are defined at the receiver point. Moreover, ERCs do not depend on the wavelet form, unlike the spherical-wave reflection coefficients. Taking into account the potential of extending ERCs to curved interfaces and arbitrary shapes of wavefronts, we exploit them to introduce long-offset AVO inversion.

ERCs for PP-waves

The PP-wave ERC for a horizontal plane interface between two homogeneous elastic half-spaces is defined as (Ayzenberg et al., 2009):

$$\chi_{PP}[\theta(\mathrm{s}_n), k_P r^*_{PP}(\mathrm{s}_n), \mathbf{m}] = \frac{u^*_{PP\,\mathrm{norm}}(\mathrm{s}_n)\cos\theta(\mathrm{s}_n) + u^*_{PP\,\tan}(\mathrm{s}_n)\sin\theta(\mathrm{s}_n)}{\left[\frac{i}{k_P r^*_{PP}(\mathrm{s}_n)} - \frac{1}{k_P^2 r^{*2}_{PP}(\mathrm{s}_n)}\right] e^{ik_P r^*_{PP}(\mathrm{s}_n)}}, \quad (3)$$

where $\mathrm{s}_n = (s_{1n}, s_{2n})$ is the reflection point, $k_P = \omega/V_{\mathrm{P1}}$ is the wavenumber in the overburden, $r^*_{PP}(\mathrm{s}_n)$ is the apparent radius of the wavefront at the reflection point, $\theta(\mathrm{s}_n)$ is the incidence angle, and $u^*_{PP\,\mathrm{norm}}(\mathrm{s}_n)$ and $u^*_{PP\,\tan}(\mathrm{s}_n)$ are the dimensionless normal and tangential components of the displacement vector. A general form of the radius $r^*_{PP}(\mathrm{s}_n)$ is introduced by Ayzenberg et al. (2007). For plane interfaces between homogeneous media, $r^*_{PP}(\mathrm{s}_n)$ reduces to the distance $l(\mathrm{s}_n)$ between the source and the reflection point. The components of the dimensionless displacement vector have the following form:

$$u^*_{PP\,\mathrm{norm}}(\mathrm{s}_n) = -\int_0^{+\infty} R_{PP}(\zeta, \mathbf{m}) e^{i\alpha(\mathrm{s}_n)\sqrt{1-\zeta^2}} J_0[\beta(\mathrm{s}_n)\zeta]\zeta \mathrm{d}\zeta,$$

$$u^*_{PP\,\tan}(\mathrm{s}_n) = -\int_0^{+\infty} R_{PP}(\zeta, \mathbf{m}) \frac{i e^{i\alpha(\mathrm{s}_n)\sqrt{1-\zeta^2}}}{\sqrt{1-\zeta^2}} J_1[\beta(\mathrm{s}_n)\zeta]\zeta^2 \mathrm{d}\zeta, \quad (4)$$

where $R_{PP}(\zeta, \mathbf{m})$ is the exact PWRC, $\alpha(\mathrm{s}_n) = k_P r^*_{PP}(\mathrm{s}_n)\cos\theta(\mathrm{s}_n)$, $\beta(\mathrm{s}_n) = k_P r^*_{PP}(\mathrm{s}_n)\sin\theta(\mathrm{s}_n)$, ζ is the horizontal component of the unit P-wave ray vector in the overburden, and J_0 and J_1 are the Bessel functions of the zeroth and first orders. We observe that because of the plane-wave decomposition in equations 3 and 4, the plane waves belonging to the Fresnel zone of the reflection point contribute to the ERC in formula 3 at this reflection point. ERCs thus represent a generalization of PWRCs for waves with the wavefronts other than plane.

In contrast to PWRC, equations 3 and 4 depend on an additional dimensionless argument $k_P r^*_{PP}(\mathrm{s}_n) = \frac{\omega_0 r^*_{PP}(0)}{V_{\mathrm{P1}}} \frac{\omega}{\omega_0} \frac{r^*_{PP}(\mathrm{s}_n)}{r^*_{PP}(0)}$, where ω_0 is the dominant frequency. The argument is a hyperbolic function of offset and has a minimum at zero offset. It describes the

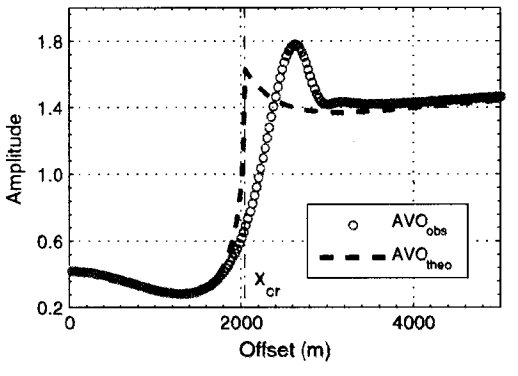

Figure 1. AVO data and its theoretical description based on the PWRC.

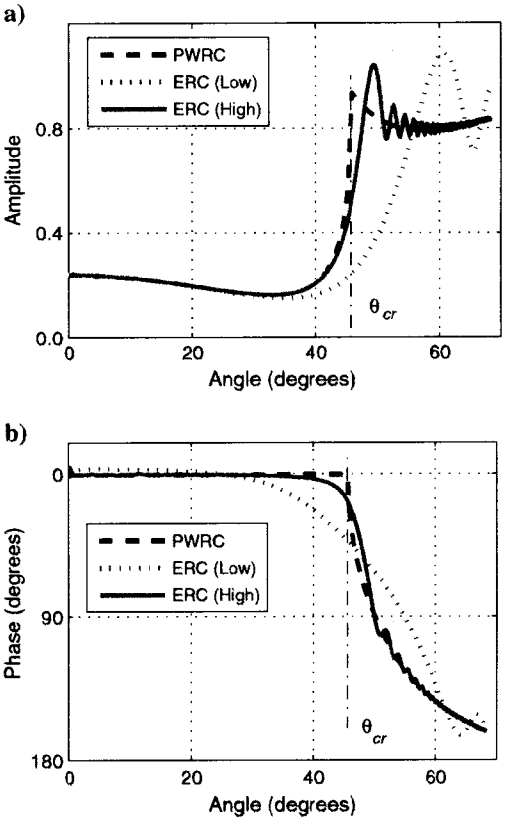

Figure 2. ERC as function on the incidence angle for $k_P r^*_P(0) = 402$ (High) and $k_P r^*_P(0) = 25$ (Low): (a) Amplitude; (b) Phase. PWRC is shown for comparison.

frequency and wavefront curvature dependence of the ERC. Depending on the value of $k_P r^*_{PP}(0)$, we distinguish three domains: a near-field domain (<1), a transition zone (1–10), and a far-field domain (>10). Assuming a seismic frequency range of 8–60 Hz, an interface depth range of 1–4 km, and P-wave velocity in the overburden of 2 km/s, we estimate that $k_P r^*_{PP}(0)$ at zero offset changes from 25 to 750. The values of $k_P r^*_{PP}(s_n)$ increase with increasing offset.

Figure 2 shows the effect of $k_P r^*_{PP}(s_n)$ on the amplitude and phase of the ERC. The P-wave velocities in upper and lower layers are 2.0 km/s and 2.8 km/s, the values of $k_P r^*_P(0)$ are 25 and 400, which are equivalent to interface depths of 1 km and frequencies of

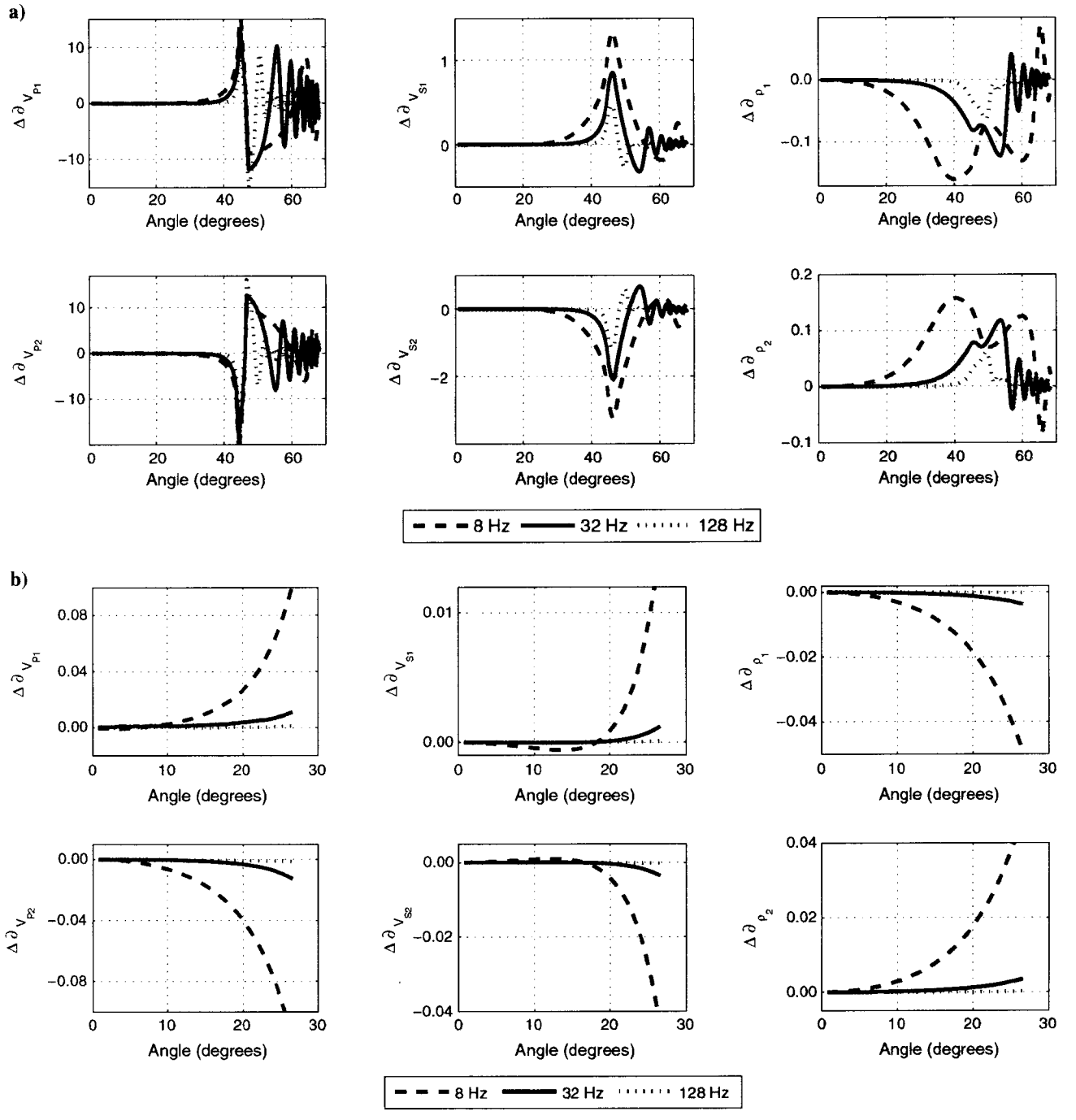

Figure 3. (a) Difference in sensitivity curves between the ERC and the PWRC; (b) zoom of (a) for an angle range of 0°–30°. Each panel shows the sensitivity to one parameter, while the rest of the parameters are set to the true model parameters. The ERC is calculated for frequencies 8, 32, and 128 Hz and an interface depth of 1 km.

8 and 128 Hz or frequency of 32 Hz and interface depths of 240 m and 4 km. Comparison of the ERC with the corresponding PWRC shows that the frequency and wavefront curvature affects the amplitude and phase of the ERC mostly at the near-critical and post-critical offsets. Although $k_P r^*_{PP}(0)$ belongs to the far-field domain, we still observe its effect at the pre-critical offsets, where the phase deviates from zero. The difference between the ERC and the PWRC decreases for larger $k_P r^*_{PP}(0)$, which is equivalent to higher frequencies or smaller wavefront curvatures. However, the ERC will still oscillate in the post-critical domain even for unrealistically large values of $k_P r^*_{PP}(0)$. ERCs describe the interference between the reflected and head wave around the critical angle, and are thus convenient for AVO inversion in the interference domain.

Argument $k_P r^*_{PP}(\mathrm{s}_n)$ depends on the velocity, frequency, and wavefront curvature. It is therefore impossible to discriminate between the three parameters in the absence of additional information. To illustrate the sensitivity of ERCs and PWRCs to the model parameters, we compute their normalized partial derivatives for a model with the following parameters; $V_{\mathrm{P1}} = 2000$ m/s, $V_{\mathrm{S1}} = 1100$ m/s, $\rho_1 = 1800$ kg/m^3 in the overburden and $V_{\mathrm{P2}} = 2800$ m/s, $V_{\mathrm{S2}} = 1600$ m/s, $\rho_2 = 2100$ kg/m^3 in the underburden. The differences between the normalized derivatives of the ERC calculated for an interface at a depth of 1 km and frequencies of 8, 32, and 128 Hz, and the corresponding PWRC, are plotted in Figure 3. Figure 3a predicts a high sensitivity at the near-critical and post-critical offsets. Each panel represents the change in one parameter, while the other parameters are set to the true model parameters. A larger difference between the derivatives means a more accurate estimate of the respective parameter. The highest sensitivity is observed for the P-wave velocities. This confirms a common understanding that the P-wave velocity can be accurately inverted for. The least accuracy is expected for densities. We notice also that the ERC is more sensitive to the P-wave and S-wave velocities in the lower layer than in the upper layer. The differences become smaller with increasing frequency. Figure 3b is the zoom of Figure 3a at the pre-critical offsets. We observe that the difference between the derivatives of the ERC and PWRC is not zero, and increases with decreasing frequency, which indicates that the results of the ERC-based and the PWRC-based AVO inversion will be different even at the pre-critical offsets. We observe a generally higher sensitivity of the ERC to the P-wave velocities, while the sensitivity to the other parameters is somewhat lower.

According to the Buckingham pi-theorem (Bluman and Kumei, 1989), we can theoretically recover five parameters from an ERC-based AVO inversion, because ERC depends on five dimensionless parameters $\frac{\rho_2}{\rho_1}$, $\frac{V_{\mathrm{P2}}}{V_{\mathrm{P1}}}$, $\frac{V_{\mathrm{S1}}}{V_{\mathrm{P1}}}$, $\frac{V_{\mathrm{S2}}}{V_{\mathrm{P2}}}$, $\frac{\alpha_0 r^*_{PP}(0)}{V_{\mathrm{P1}}}$. Assuming the dominant frequency and the $r^*_{PP}(0)$ in last parameter to be known, we can decouple and resolve all four velocities V_{P1}, V_{S1}, V_{P2}, V_{S2}. Densities can be decoupled only if one of them is available.

LONG-OFFSET AVO INVERSION

Approximate description of a single reflection at the receiver

Ayzenberg et al. (2009) have shown that the reflected seismic wavefield at a curved interface can be approximately described in terms of ERCs. Skopintseva et al. (2007) have numerically verified that the P-wave reflected at a plane interface can be described in terms of ERCs both at the interface and at the receiver. We derive a seismic frequency approximation of the reflected P-wave at the receiver in terms of the ERC and show that it has a form convenient for AVO studies (Appendix A):

$$\mathbf{u}_{PP}(\mathrm{x}_n, \omega) \cong \chi_{PP}[\mathrm{x}_n, \omega] \frac{i}{V_{\mathrm{P1}}} S(\omega) \frac{e^{ik_P l(\mathrm{x}_n)}}{\sqrt{J_{PP}(\mathrm{x}_n)}} \mathbf{e}_{PP}(\mathrm{x}_n), \quad (5)$$

where $\chi_{PP}[\mathrm{x}_n, \omega] = \chi_{PP}[\theta(\mathrm{x}_n), k_P r^*_{PP}(\mathrm{x}_n), \mathbf{m}]$ is the ERC defined at the receiver, $l(\mathrm{x}_n) = l(\mathrm{x}_n, \mathrm{s}_n) + l(\mathrm{s}_n)$ is the distance between the source and receiver x_n along the ray, $l(\mathrm{x}_n, \mathrm{s}_n)$ is the distance between the reflection point and the receiver, $l(\mathrm{s}_n)$ is the distance between the source and the reflection point, $J_{PP}(\mathrm{x}_n) = [l(\mathrm{x}_n)]^2$ is the geometrical spreading of the reflected P-wave, $S(\omega)$ is the wavelet spectrum, and $\mathbf{e}_{PP}(\mathrm{x}_n)$ is the polarization vector of the reflected P-wave. Equation 5 resembles the wavefield representation from asymptotic ray theory, where the PWRC is substituted by the ERC at the receiver. Extrapolation of the ERC from the interface to the receiver is performed with help of the relation $r^*_{PP}(\mathrm{x}_n) = r^*_{PP}(\mathrm{s}_n)[1 + l(\mathrm{x}_n, \mathrm{s}_n)/l(\mathrm{s}_n)]$.

Equation 5 in the time domain has the following form:

$$\mathbf{U}_{PP}(\mathrm{x}_n, t) \cong \frac{i}{V_{\mathrm{P1}}} \frac{\mathbf{e}_{PP}(\mathrm{x}_n)}{\sqrt{J_{PP}(\mathrm{x}_n)}} \int_{-\infty}^{+\infty} \chi_{PP}[\mathrm{x}_n, \omega] S(\omega) e^{i\{k_P l(\mathrm{x}_n) - \omega t\}} \mathrm{d}\omega, \quad (6)$$

where $\mathbf{U}_{PP}(\mathrm{x}_n, t) = (U_{PPX}(\mathrm{x}_n, t), 0, U_{PPZ}(\mathrm{x}_n, t))$ is the displacement vector, and $\mathbf{e}_{PP}(\mathrm{x}_n) = (\sin\theta(\mathrm{x}_n), 0, \cos\theta(\mathrm{x}_n))$ is the polarization vector.

Band-limited AVO data and its theoretical description

We further consider the preprocessed AVO data, where the geometrical spreading is removed:

$$\tilde{\mathbf{U}}_{PP}(\mathrm{x}_n, t) = \sqrt{J_{PP}(\mathrm{x}_n)}\mathbf{U}_{PP}(\mathrm{x}_n, t),$$
$$\tilde{\mathbf{u}}_{PP}(\mathrm{x}_n, \omega) = \sqrt{J_{PP}(\mathrm{x}_n)}\mathbf{u}_{PP}(\mathrm{x}_n, \omega). \quad (7)$$

Based on the property $\tilde{\mathbf{u}}_{PP}(\mathrm{x}_n, -\omega) = \bar{\tilde{\mathbf{u}}}_{PP}(\mathrm{x}_n, +\omega)$ of the spectrum of a real function, we write Parseval's theorem for the reflected wavefield $\tilde{\mathbf{U}}_{PP}(\mathrm{x}_n, t)$ and its spectrum $\tilde{\mathbf{u}}_{PP}(\mathrm{x}_n, \omega)$ (Korn and Korn, 1968):

$$\int_{-\infty}^{\infty} [\tilde{U}_{PPj}(\mathrm{x}_n, t)]^2 dt = 2\int_0^{\infty} \tilde{u}_{PPj}(\mathrm{x}_n, \omega)\bar{\tilde{\mathbf{u}}}_{PPj}(\mathrm{x}_n, \omega)\mathrm{d}\omega, \quad (8)$$

where the bar denotes a complex conjugation, $j = X, Z$ for the X- and Z-components of the reflected wavefield $\tilde{\mathbf{U}}_{PP}(\mathrm{x}_n, t) = (\tilde{U}_{PPX}(\mathrm{x}_n, t), 0, \tilde{U}_{PPZ}(\mathrm{x}_n, t))$. The left part of the equation represents the squared rms value over an infinite time window. We define a finite time window $[t_1(\mathrm{x}_n), t_2(\mathrm{x}_n)]$ which follows the moveout of the reflected event. Substituting equation 5 and 7 to 8, we represent the rms amplitudes for the X- and Z-components of the reflected wavefield though the ERC:

$$\left(\int_{t_1(\mathrm{x}_n)}^{t_2(\mathrm{x}_n)} [\tilde{U}_{PPj}(\mathrm{x}_n, t)]^2 \mathrm{d}t\right)^{\frac{1}{2}}$$
$$= \frac{\sqrt{2}}{V_{\mathrm{P1}}} |e_{PPj}(\mathrm{x}_n)| \sqrt{\int_{\omega_{\min}}^{\omega_{\max}} |S(\omega)|^2 |\chi_{PP}[\mathrm{x}_n, \omega]|^2 \mathrm{d}\omega}. \quad (9)$$

Equation 9 incorporates all ERCs whose frequencies are within the frequency range $[\omega_{\min}, \omega_{\max}]$. Moreover, the ERCs are weighted

with the amplitude spectrum of the wavelet. Figure 4 shows the effect of weighting for three randomly chosen frequencies of the wavelet. We observe that the main contribution is obtained from the ERC calculated for the dominant frequency ω_0. The ERCs for the neighboring frequencies affect only the oscillations at the post-critical angles. The oscillations are suppressed when a wider frequency range is involved in the weighting.

The factor $\sqrt{2}/V_{\mathrm{PI}}$ in equation 9 does not depend on the offset and can be eliminated through a normalizing procedure over the full offset range. Applying the normalizing procedure to the left and right parts of equation 9, we obtain the AVO data and its corresponding theoretical description:

$$AVO_{\mathrm{obs}\,j}(\mathrm{x}_n) = \frac{\left(\int_{t_1(\mathrm{x}_n)}^{t_2(\mathrm{x}_n)} [\tilde{U}_{PPj}(\mathrm{x}_n, t)]^2 \mathrm{d}t\right)^{\frac{1}{2}}}{\frac{1}{N}\sum_{n=1}^{N}\left(\int_{t_1(\mathrm{x}_n)}^{t_2(\mathrm{x}_n)} [\tilde{U}_{PPj}(\mathrm{x}_n, t)]^2 \mathrm{d}t\right)^{\frac{1}{2}}}$$

$$AVO_{\mathrm{theo}\,j}(\mathrm{x}_n) = \frac{|e_{PPj}(\mathrm{x}_n)|\sqrt{\int_{\omega_{\min}}^{\omega_{\max}} |S(\omega)|^2 |\chi_{PP}[\mathrm{x}_n, \omega]|^2 \mathrm{d}\omega}}{\frac{1}{N}\sum_{n=1}^{N}\left(|e_{PPj}(\mathrm{x}_n)|\sqrt{\int_{\omega_{\min}}^{\omega_{\max}} |S(\omega)|^2 |\chi_{PP}[\mathrm{x}_n, \omega]|^2 \mathrm{d}\omega}\right)}, \quad (10)$$

where $j = X, Z$ for the X- and Z-components of the reflected P-wave. Based on these equations, AVO inversion can be performed on either component of the reflected P-wave data. If both components are available, equations 10 can be represented as

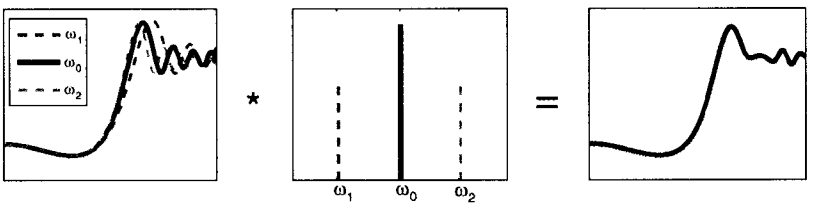

Figure 4. A scheme explaining the process of computing the theoretical description of the band-limited AVO data. From left to right: ERCs for three different frequencies, amplitude spectrum of the source wavelet, and the result after weighting and averaging.

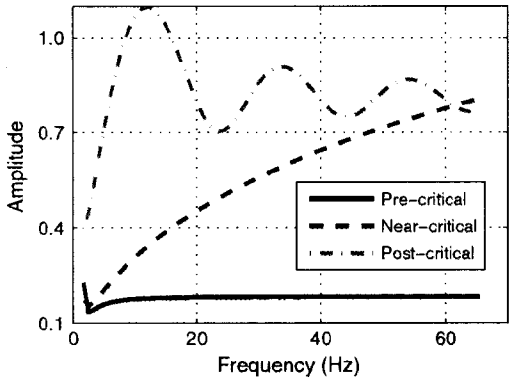

Figure 5. ERC as function of frequency for pre-critical, near-critical, and post-critical offsets.

$$AVO_{\mathrm{obs}}(\mathrm{x}_n) = \frac{\left(\int_{t_1(\mathrm{x}_n)}^{t_2(\mathrm{x}_n)} [\tilde{U}_{PP}(\mathrm{x}_n, t)]^2 \mathrm{d}t\right)^{\frac{1}{2}}}{\frac{1}{N}\sum_{n=1}^{N}\left(\int_{t_1(\mathrm{x}_n)}^{t_2(\mathrm{x}_n)} [\tilde{U}_{PP}(\mathrm{x}_n, t)]^2 \mathrm{d}t\right)^{\frac{1}{2}}}$$

$$AVO_{\mathrm{theo}}(\mathrm{x}_n) = \frac{\sqrt{\int_{\omega_{\min}}^{\omega_{\max}} |S(\omega)|^2 |\chi_{PP}[\mathrm{x}_n, \omega]|^2 \mathrm{d}\omega}}{\frac{1}{N}\sum_{n=1}^{N}\sqrt{\int_{\omega_{\min}}^{\omega_{\max}} |S(\omega)|^2 |\chi_{PP}[\mathrm{x}_n, \omega]|^2 \mathrm{d}\omega}}, \quad (11)$$

where $\tilde{U}_{PP}(\mathrm{x}_n) = \sqrt{\tilde{U}^2_{PPX}(\mathrm{x}_n) + \tilde{U}^2_{PPZ}(\mathrm{x}_n)}$ is the magnitude of the displacement vector. In this case, $AVO_{\mathrm{theo}}(\mathrm{x}_n)$ does not require computation of the polarization vector.

We note that the theoretical description of the AVO data in equations 10 and 11 requires knowledge about the wavelet spectrum $S(\omega)$. We find the X- and Z-components of the power spectrum of the reflected wavefield in terms of the wavelet spectrum from equations 5 and 7:

$$|S^D_j(\mathrm{x}_n, \omega)| = \sqrt{\tilde{u}_{PPj}(\mathrm{x}_n, \omega)\bar{\tilde{u}}_{PPj}(\mathrm{x}_n, \omega)} = \frac{|e_{PPj}(\mathrm{x}_n)|}{V_{\mathrm{PI}}}|S(\omega)||\chi_{PP}[\mathrm{x}_n, \omega]|, \quad (12)$$

where $j = X, Z$ and $\tilde{\mathbf{u}}_{PP}(\mathrm{x}_n, \omega) = (\tilde{u}_{PPX}(\mathrm{x}_n, \omega), 0, \tilde{u}_{PPZ}(\mathrm{x}_n, \omega))$.

Figure 5 demonstrates the frequency dependence of the ERC magnitude for three chosen offsets corresponding to pre-critical, near-critical, and post-critical domains. We observe that the ERC weakly depends on the frequency at the pre-critical offsets, while the frequency dependence becomes more prominent at the near-critical and post-critical offsets. We can therefore exploit the power spectrum $|S^D(\mathrm{x}_{\mathrm{pre}}, \omega)|$ at any pre-critical offset in equations 10 and 12 instead of the wavelet spectrum $|S(\omega)|$. This does not affect the result because of the following relationship

$$|S^D_j(\mathrm{x}_{\mathrm{pre}}, \omega)| = \frac{|e_{PPj}(\mathrm{x}_{\mathrm{pre}})|}{V_{\mathrm{PI}}}|S(\omega)||\chi_{PP}[\mathrm{x}_{\mathrm{pre}}, \omega]| \approx C|S(\omega)|, \quad (13)$$

where C is a constant which is eliminated through a normalization procedure. The power spectrum of the data can only serve as a proxy for the spectrum of the wavelet if there is no significant frequency dependence in the ERC at the pre-critical offsets. This may be not the case in attenuative media.

Because the considered AVO data includes all frequencies present in the reflected wavefield, we refer to $AVO_{\mathrm{obs}}(\mathrm{x}_n)$ and $AVO_{\mathrm{theo}}(\mathrm{x}_n)$ as the band-limited AVO data and its theoretical description, respectively.

Single-frequency AVO data and its theoretical representation

An alternative way to obtain AVO data from the surface seismic data is based on equation 12. Applying the normalization procedure to the left and right parts of equation 12, we obtain the representation of the AVO data for each component of the reflected wavefield and their theoretical description in the frequency domain:

$$AVO_{\mathrm{obs}j}(\mathrm{x}_n,\omega)=\frac{\sqrt{\tilde{u}_{PPj}(\mathrm{x}_n,\omega)\bar{\tilde{u}}_{PPj}(\mathrm{x}_n,\omega)}}{\frac{1}{N}\sum_{n=1}^{N}\sqrt{\tilde{u}_{PPj}(\mathrm{x}_n,\omega)\bar{\tilde{u}}_{PPj}(\mathrm{x}_n,\omega)}}$$

$$AVO_{\mathrm{theo}j}(\mathrm{x}_n,\omega)=\frac{|e_{PPj}(\mathrm{x}_n)||\chi_{PP}[\mathrm{x}_n,\omega]|}{\frac{1}{N}\sum_{n=1}^{N}|e_{PPj}(\mathrm{x}_n)||\chi_{PP}[\mathrm{x}_n,\omega]|}. \quad (14)$$

Similarly to equation 11, equation 14 can be rewritten in terms of displacements $\tilde{u}_{PP}(\mathrm{x}_n,\omega)=\sqrt{\tilde{u}^2_{PPX}(\mathrm{x}_n,\omega)+\tilde{u}^2_{PPZ}(\mathrm{x}_n,\omega)}$ in the frequency domain:

$$\mathrm{AVO}_{\mathrm{obs}}(\mathrm{x}_n,\omega)=\frac{\sqrt{\tilde{u}_{PP}(\mathrm{x}_n,\omega)\bar{\tilde{u}}_{PP}(\mathrm{x}_n,\omega)}}{\frac{1}{N}\sum_{n=1}^{N}\sqrt{\tilde{u}_{PP}(\mathrm{x}_n,\omega)\bar{\tilde{u}}_{PP}(\mathrm{x}_n,\omega)}}$$

$$\mathrm{AVO}_{\mathrm{theo}}(\mathrm{x}_n,\omega)=\frac{|\chi_{PP}[\mathrm{x}_n,\omega]|}{\frac{1}{N}\sum_{n=1}^{N}|\chi_{PP}[\mathrm{x}_n,\omega]|}. \quad (15)$$

AVO data from equations 14 and 15 can be obtained for an arbitrary frequency within the range $[\omega_{\min},\omega_{\max}]$. This gives us the freedom to extract AVO data from the reflected wavefield for particular frequencies. The theoretical description of AVO data is simpler, as it does not require any knowledge about the wavelet spectrum. It can be interpreted as a normalized ERC. The absence of integration allows to reduce the computational cost of the AVO inversion.

We refer to $AVO_{\mathrm{obs}}(\mathrm{x}_n,\omega)$ and $AVO_{\mathrm{theo}}(\mathrm{x}_n,\omega)$ as the single-frequency AVO data and its theoretical description.

AVO INVERSION OF LONG-OFFSET SYNTHETIC DATA

To test the described AVO inversion approach, we use 3D long-offset synthetic PP data obtained from elastic reflectivity modeling. The tests are carried out for two models with a flat horizontal interface between two homogeneous isotropic half-spaces. We generate the seismograms for the X- and Z-components. For simplicity we consider common-shot gathers, which in the case of a plane interface are equivalent to CDP gathers with half the distance between the source and the receivers. The source and receiver array are located at the surface. The receiver sampling is 25 m.

We exploit an omnidirectional source with the wavelet $S(t)=-\frac{\partial}{\partial t}\exp^{-((2\pi ft)/\pi)^2}\sin(2\pi ft)$, where t is time and $f=\omega/2\pi$ is the linear frequency. The wavelet has an amplitude spectrum $S(f)$ with a bell-like envelope, the frequencies ranging from $f_{\min}=3$ Hz to $f_{\max}=62$ Hz, and a dominant linear frequency of 39 Hz.

Model 1

The first test is performed for an interface located 1 km below the source. The upper half-space is described by the parameters $V_{P1}=2000$ m/s, $V_{S1}=1100$ m/s, $\rho_1=1800$ kg/m^3, and the lower half-space is described by the parameters $V_{P2}=2800$ m/s, $V_{S2}=1600$ m/s, $\rho_2=2100$ kg/m^3. The critical angle for this model is equal to 45.6°, and the critical offset is $\mathrm{x}_{cr}=2041$ m. The offsets vary from 0 to 5000 m and cover pre-critical, near-critical, and post-critical reflections.The value of argument $k_{Pr}r^*_{PP}(\mathrm{x}_n)$ at minimal frequency 3 Hz changes from 18 at zero offset to 60 at offset 5000 m, respectively. The value of this argument at maximal frequency 60 Hz changes from 584 at zero offset to 1246 at offset 5000 m, respectively. The argument $k_{Pr}r^*_{PP}(\mathrm{x}_n)$ at dominant frequency of 39 Hz changes from 245 to 784 at zero and maximum offsets, respectively.

The seismogram of the Z-component obtained by reflectivity modeling is shown in Figure 6a. We observe a significant amplitude increase at the offsets above 2000 m. A weak head wave is present on the seismogram and separates from the reflected wave at long offsets. The amplitude of the wavelet spectrum is shown in Figure 6b.

AVO data and its theoretical representation

To obtain the band-limited AVO data, we apply the first equation in 11 to the X- and Z-components of the data compensated for the geometrical spreading.

To obtain the single-frequency AVO data, we apply the temporal Fourier transform to the X- and Z-components of the seismogram corrected for the geometrical spreading and use the first equation in 15. Figure 7 shows the single-frequency AVO data for all frequencies contained in the wavelet spectrum. The effect of the critical angle becomes prominent for the offsets above 2000 m. The rapid oscillations at the post-critical offsets are explained by the interference of the reflected and head waves. Moreover, we observe that the position of the amplitude maximum at the post-critical offsets depends on the frequency and tends to the critical offset with increasing frequency, while the amplitude at the pre-critical offsets is close to being frequency-independent.

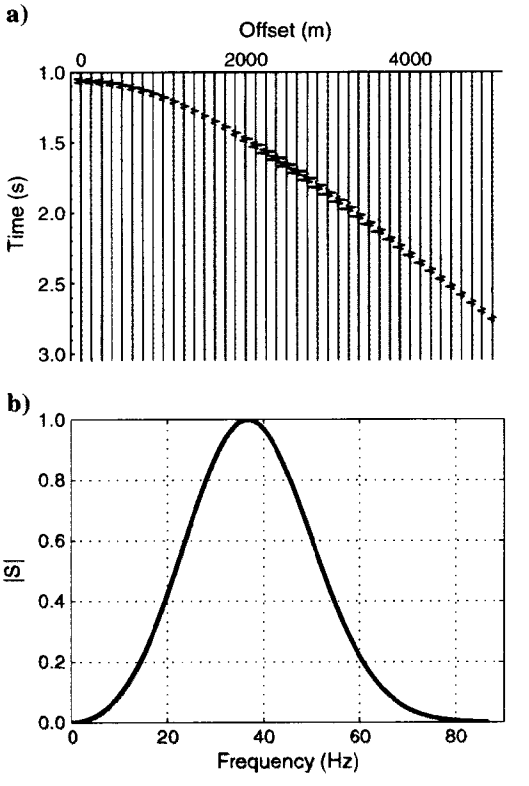

Figure 6. (a) Z-component of the reflected P-wave obtained from the reflectivity modeling; (b) Wavelet spectrum.

Figure 8 shows the slice of the single-frequency AVO data for a frequency of 32 Hz, the band-limited AVO data, and the corresponding theoretical descriptions calculated for the true model parameters. The ERC-based theoretical descriptions are obtained from the second equations in 15 and 11. In equation 15, we assume that the wavelet spectrum $|S(\omega)|$ is unknown and use the amplitude spectrum $|S^D(x_{pre}, \omega)|$ from the data at a pre-critical offset of 1500 m. We show also the PWRC-based theoretical description (equation 2) for comparison.

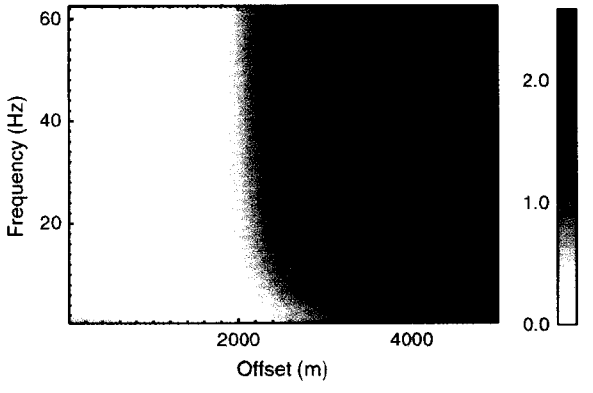

Figure 7. Single-frequency AVO data.

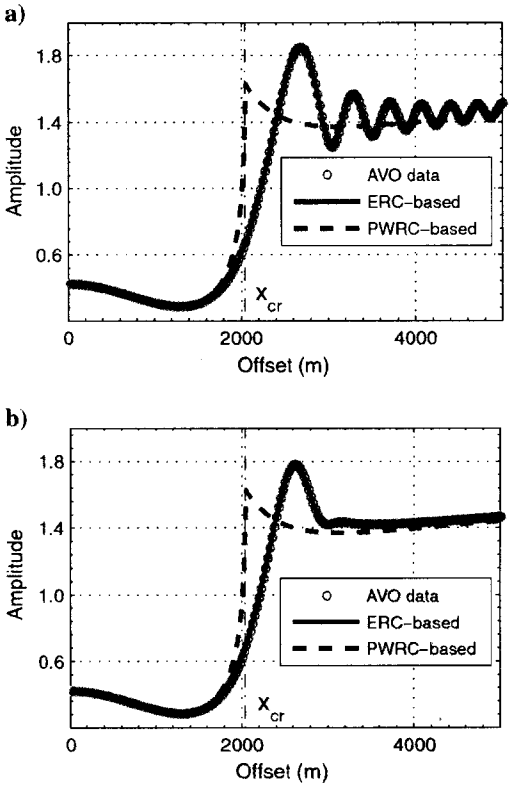

Figure 8. AVO data and their theoretical descriptions calculated for the true model parameters. (a) Single-frequency AVO data for 32 Hz (circles), ERC-based single-frequency theoretical description for 32 Hz (solid line), and PWRC-based theoretical description (dashed line); (b) Band-limited AVO data (circles), ERC-based band-limited theoretical description (solid line), and PWRC-based theoretical description (dashed line).

The single-frequency AVO data exhibit strong oscillations at the post-critical offsets, whereas such oscillations are absent in the band-limited AVO data because of the averaging over frequencies, as illustrated in Figure 4. The ERC-based theoretical description resembles the AVO data at all offsets, whereas the PWRC-based description coincides with the AVO data only at the pre-critical offsets, and substantially deviates from it at the near-critical and post-critical offsets. Based on this observation, we may expect that the PWRC-based inversion will produce similar level of errors in parameter estimates to the ERC-based inversion at pre-critical offsets. At the same time, we expect a different behavior of errors with offset due to $k_P r^*_{PP}(x_n)$, which enhances the sensitivity of the ERC to media parameters compared to the PWRC. We may expect that the ERC-based inversion will outperform the PWRC-based inversion at the near-critical and post-critical offsets.

Analysis of the objective functions

We examine the shape of the objective functions to understand the potential of the ERC-based and PWRC-based AVO inversions for parameter recovery at different offset ranges.

Figure 9 shows 2D crossplots of the objective function $F(\mathbf{v})$ (equation 1), where we vary only two parameters while the rest are set to the true model parameters. The deviation of varying parameters from their true value is ±20%. The first two columns represent maps of $F(V_{P1}, \rho_1)$ and $F(V_{S2}, \rho_1)$ computed from the ERC-based band-limited AVO data and the band-limited theoretical description. The last two columns show the same maps computed from the single-frequency AVO data and its ERC-based theoretical description (equation 15). The first row represents the maps computed for the pre-critical offset range 0–1500 m (0°–36°), whereas the second one shows the maps computed for the full offset range 0–5000 m (0°–68°). The circles denote the minimum of the objective function, while the squares indicate the true model parameters.

We observe that the behavior of the objective functions is different for the pre-critical and the full offset ranges. The objective function does not have well-defined minima for the pre-critical offset range, whereas they become more isometric with increasing offset range. This is explained by the different sensitivity of the ERC to parameters at different offsets ranges. Stronger amplitudes at long offsets contribute more to the objective functions. We observe also that all the functions are most uncertain in the ρ_1-direction. This may result in higher uncertainties of the density estimates.

The objective functions are V-shaped and stretched in the ρ_1-direction for the pre-critical offsets. The minima of the objective functions coincide with the true model parameters on almost all the maps, except for the $F(V_{P1}, \rho_1)$ for the single-frequency AVO data, where the deviation in the V_{P1}-direction is less than in the ρ_1-direction. This can probably be explained by the computational errors in the data at short offsets. We do not observe significant deviations for the band-limited case because the band-limited theoretical data AVO_{theo} is more robust to the computational errors because of averaging over frequencies. Such behavior of the objective functions and the deviation of the minima may lead to unstable inversion results at the pre-critical offsets. We also expect more accurate results from the band-limited AVO inversion than from the single-frequency AVO inversion. The objective functions for

the full offset range exhibit a good fit between the minima of the objective functions and the true model parameters. We therefore claim that the near-critical and post-critical offsets will increase the accuracy of parameter estimation.

We additionally analyze maps of the objective functions $F(V_{P1}, \rho_1)$ and $F(V_{S2}, \rho_1)$ evaluated using the PWRC-based theoretical description instead of the band-limited and single-frequency descriptions (Figure 10). The deviation of varying parameters from their true value is ±40%. In this case, we observe a more complex behavior of the objective functions than those in Figure 9. The misfits between the minima of the objective functions and the true model parameters at the pre-critical offsets are explained by the wavefront curvature present in the data, while it is not accounted for in the PWRC-based theoretical description. This will lead to less accurate parameter estimates. We observe also that incorporation of the near-critical and post-critical offsets does not improve the shapes of the objective functions. There are still significant deviations of the positions of the minima from the true model parameters.

Figure 11 compares the ERC-based and the PWRC-based 1D objective functions for band-limited AVO data in the vicinity of their minimum. The computation is carried out for a pre-critical offset range of 0–1500 m. Despite the fact that the amplitudes of the ERC and the PWRC are almost equal, we observe that the PWRC-based objective function is asymmetric and its minimum is shifted from the true value. This confirms that the ERC-based and the PWRC-based AVO inversions will perform differently even at the pre-critical offsets.

AVO inversion results

To include post-critical offsets in the inversion, we use the exact reflection coefficients (ERCs or PWRCs), which imply nonlinear inversion methods. Among the existing optimization methods, we chose the nonlinear optimization method of Nelder-Mead for minimizing the objective function in equation 1 (Himmelblau, 1972). The method is computationally simple and effective, because it does not require calculation of partial derivatives. However, we need to provide an initial guess for the estimated parameters. A good starting model ensures fast convergence of the inversion to the final result. An initial guess is typically obtained from the low-frequency velocity trends and rock-physical relationships. In our case the objective function has only one minimum for the parameter deviation within 20%. The initial guess can therefore belong to this range.

We carried out AVO inversion for offset ranges varying from 0 to 250 m to 0–5000 m with an increment of 250 m. We allowed for a 20% variation in the estimated parameters. The initial guess deviates by 15% from the true model parameters. Figure 12 illustrates the results of the single-frequency ERC-based AVO inversion, where we invert for the five-parameter vector $\mathbf{v} = (V_{P1}, V_{S1}, V_{P2}, V_{S2}, \rho_1)$ assuming the density ρ_2 in the underburden to be known. The inversion results are plotted as functions of the offset range. As expected, we see that increase in the offset range generally improves the inversion results. All the parameters are estimated more accurately when the post-critical offsets are involved in the inversion. The best accuracy is achieved for the P-wave velocities and the density ρ_1, while the S-wave velocities are less accurate. At pre-critical offset ranges (until 2000 m), the S-wave velocity and P-wave velocity in the underburden and density are estimated better than the other two parameters. The accuracy of V_{P2} is higher than the accuracy of V_{P1} at the pre-critical offsets, whereas the accuracy of their estimates is approximately the same at the post-critical offsets.

We illustrate the sensitivity of the objective function for the single-frequency AVO inversion to the model parameters by showing its normalized derivatives at different offset ranges (Figure 13). A larger derivative is associated with a better estimate

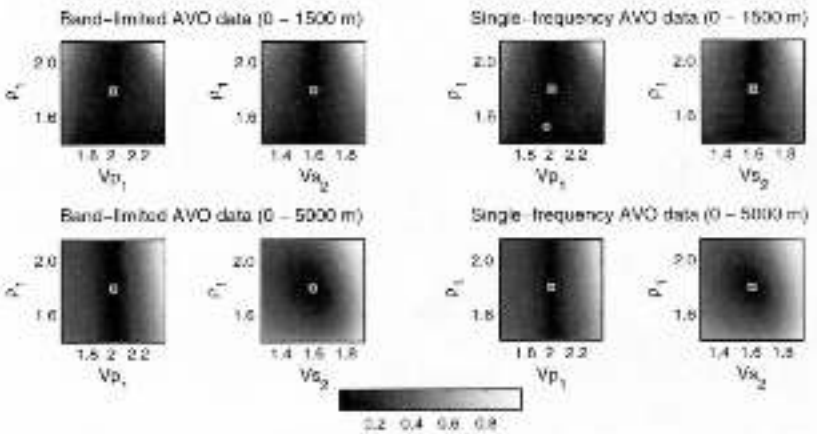

Figure 9. Cross sections of the ERC-based objective functions. The band-limited and single-frequency theoretical descriptions are used for evaluation of the band-limited and single-frequency AVO data. Squares denote true model parameters and circles denote minima of the objective functions.

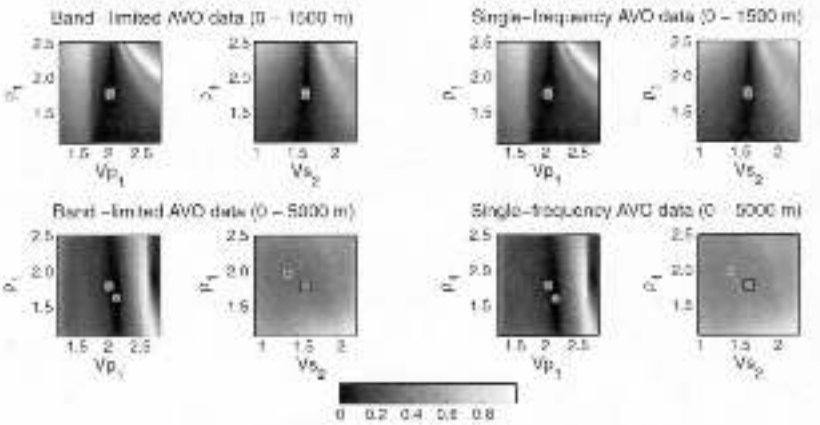

Figure 10. Cross sections of the PWRC-based objective functions. The PWRC-based theoretical description is used for evaluation of the band-limited and single-frequency AVO data. Squares denote true model parameters and circles denote minima of the objective functions.

of the inverted parameter. We observe that the derivatives with respect to V_{S2} and V_{P2} at short offset ranges forecast an accurate estimate of these parameters. The rapid increase of the derivative with respect to V_{P1} and V_{P2} at the near-critical and post-critical offsets confirms the ability of the inversion to resolve the P-wave velocities better than other parameters. The sensitivity to the densities becomes larger than the sensitivity to V_{S1} when the post-critical offsets are included in the computation. This indicates that the post-critical offsets contain additional information about the densities. These observations correlate well with the inversion results in Figure 12.

We additionally observe a zone between 2000–3000 m, where the relative behavior between the derivative curves changes and the objective function is almost equally sensitive to both P-wave velocities. This area corresponds to a local drop in the quality of estimated parameters (Figure 12). We observe that in this particular interval there is a strong correlation between the sensitivities to the two P-wave velocities. Although the Buckingham pi-theorem states that five parameters can be retrieved from the ERC-based inversion, the uniqueness of the five-parameter inversion for this particular interval is questionable and requires further study. Figure 13 explains some of the inversion results. However, it does not provide a full picture, because a nonlinear inversion is a nontrivial search for the minimum of a multidimensional objective function.

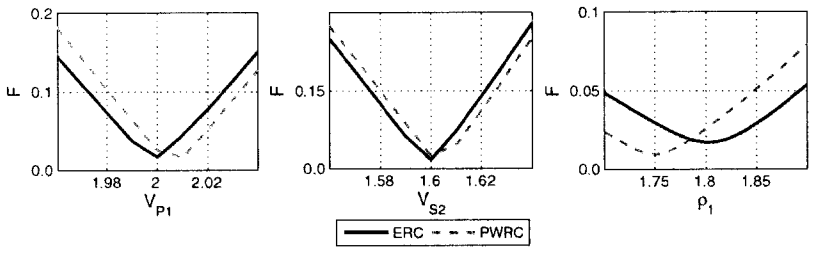

Figure 11. 1D cross sections of the objective functions based on the ERC and the PWRC. The objective functions are calculated for the band-limited AVO data at pre-critical offset range (0–1500 m).

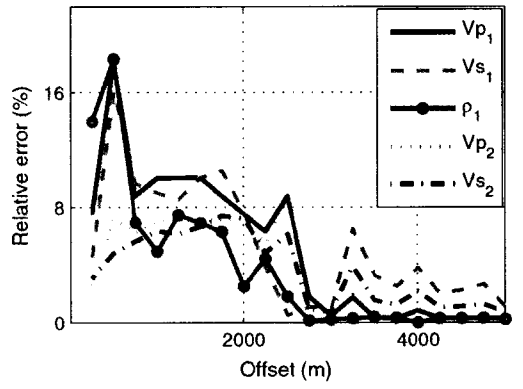

Figure 12. Relative errors in the five-parameter single-frequency (32 Hz) ERC-based AVO inversion for Model 1 as function of offset range.

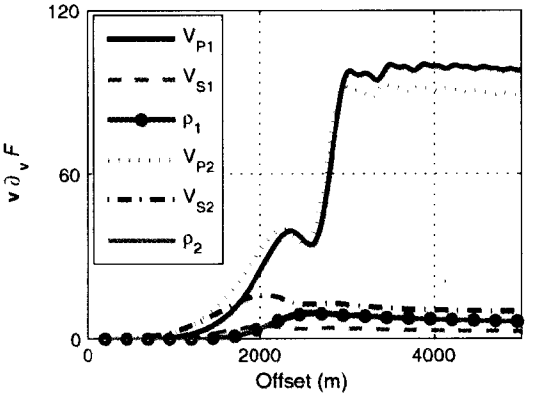

Figure 13. Normalized derivatives of the single-frequency ERC-based objective function with respect to the model parameters for different offset ranges. A higher value of the derivative with respect to a parameter corresponds to a higher sensitivity of the objective function to this parameter.

To demonstrate the improvement in the results obtained from the ERC-based AVO inversion, we compare it with the PWRC-based AVO inversion. We perform four-parameter inversions because the PWRC-based AVO inversion allows recovery of only four parameters (Lavaud et al., 1999). We assume V_{P2} and ρ_2 to be known and recover the parameter vector $\mathbf{v} = (V_{P1}, V_{S1}, \rho_1, V_{S2})$. Figure 14 illustrates the results of the four-parameter ERC-based AVO inversion as a function of the offset range. Figure 14a and 14b corresponds to the single-frequency and the band-limited AVO inversions. We observe that in both cases the accuracy of parameter estimation generally increases with increasing offset range. The results obtained at the pre-critical offset ranges are least accurate and least stable, in particular because of the short offsets and numerical errors. When proceeding from the pre-critical offsets to the near-critical offsets, the accuracy of all estimated parameters increases. We observe an increase in the error in the estimated S-wave velocities an offset range of 2000–3000 m. The effect weakens outside this zone. This is well correlated with the local minima and maxima observed in Figure 13. The P-wave velocity estimate appears to be most accurate and robust at the near-critical and post-critical offsets. The estimated S-wave velocities exhibit similar trends, but a somewhat lower accuracy. The lowest accuracy is achieved for the S-wave velocity V_{S1} in the overburden. The density estimates appear to be surprisingly good, in particular when the near-critical and post-critical offsets are included in the inversion.

Taking into account that the synthetic data contain numerical errors, we obtain an insight into the sensitivity of the ERC-based AVO inversion to the irregular noise. We observe from Figure 14a and 14b that the errors in the single-frequency AVO inversion at the pre-critical offsets are larger than those for the band-limited AVO inversion. It indicates that the latter inversion is more robust to irregular noise than the former. However, the band-limited AVO inversion implies an increase in the computational cost because of averaging over frequencies. The single-frequency AVO inversion, on the contrary, is faster and less accurate.

Figure 15 shows the inversion results obtained from the PWRC-based AVO inversion. Figure 15a and 15b corresponds to

the single-frequency and the band-limited AVO inversions. We observe that the PWRC-based AVO inversion generally produces less accurate results than the ERC-based AVO inversion. Despite the similarities between the ERC and the PWRC at the pre-critical offsets, we observe different behaviors of the relative errors in parameters estimates. The range of errors for both inversions varies between 2% and 12%. The differences are explained by the different sensitivities of the reflection coefficients to the parameters because of the additional argument $k_P r^*_{PP}(x_n)$. This explanation is supported by the shapes of the objective functions and the sensitivity study. We observe an abrupt decrease in the accuracy of all estimated parameters at the near-critical offsets. This is explained by a strong inconsistency of the plane-wave description to the AVO data at the near-critical offsets. Whenever the post-critical offsets are involved in the inversion, the error curves become flat. This indicates that increase in the offset range will not improve the quality of estimated parameters. We note also that the S-wave velocity in the overburden is least accurately estimated, regardless of the offset range. We suspect that S-wave velocities are more sensitive to errors at post-critical offsets than other parameters. Although multicomponent seismics continue to increase in popularity, single-component data is still widely acquired in the industry. We therefore provide the AVO inversion results obtained from only from the Z-component (Figure 16). We exploit equations 12 and perform the ERC-based band-limited AVO inversion. We observe that the accuracy of the parameter estimates decreases, especially at the near-critical and post-critical offsets.

The reason for a decreased accuracy is the approximation in the polarization vector of the reflected P-wave, which causes larger errors with increasing offset range. This consequently causes a shift in the minimum of the objective function. The error curves at the pre-critical offsets resemble those for the 2C AVO inversion, however, they are nearly constant at the near-critical and post-critical offsets. Although the accuracy of the P-wave velocity estimation remains high, the errors in V_{S2} and ρ_1 increase to 8% and 3%, respectively. The S-wave velocity V_{S1} in the upper layer is not resolved, because the error exceeds the 20% limit used as a starting point for the inversion. The accuracy curves show qualitatively the same behavior as the accuracy curves in Figure 13. A comparison of the 1C ERC-based and PWRC-based AVO inversions shows that the former outperforms the latter.

Model 2

To illustrate the validity of the ERC-based AVO inversion, we perform an additional test on a model with two critical angles. An interface located 0.5 km below the source separates the two half-spaces with the parameters $V_{P1} = 1300$ m/s, $V_{S1} = 800$ m/s, and $\rho_1 = 1800$ kg/m^3 in the overburden, and $V_{P2} = 2400$ m/s, $V_{S2} = 1700$ m/s, and $\rho_2 = 2100$ kg/m^3 in the

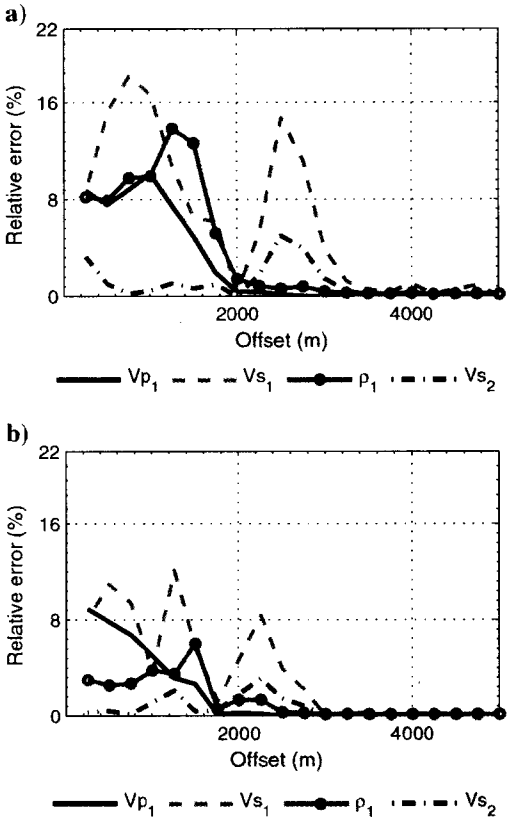

Figure 14. Relative errors in the four-parameter AVO inversion as function of the offset range for Model 1. (a) ERC-based single-frequency AVO inversion for 32 Hz; (b) ERC-based band-limited AVO inversion.

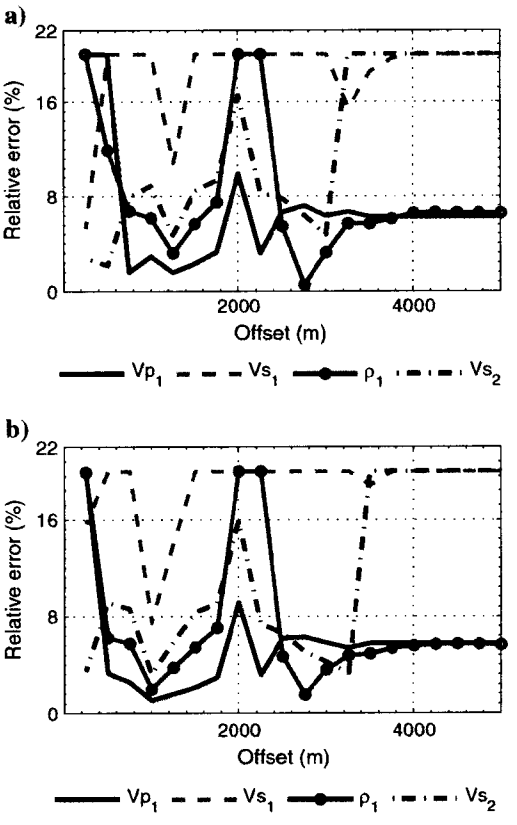

Figure 15. Relative error in the four-parameter AVO inversion as function of the offset range for Model 1. (a) PWRC-based single-frequency AVO inversion for 32 Hz; (b) PWRC-based band-limited AVO inversion.

underburden. The first critical angle $\theta_{cr1} = 32.8°$ (corresponding to a critical distance of $x_{cr1} = 644$ m) generates a PPP-type head wave. The second critical angle $\theta_{cr1} = 49.9°$ (corresponding to a critical distance of $x_{cr2} = 1187$ m) creates a converted PSP-type head wave. The receiver offsets vary from 0 to 2500 m and cover the pre-critical, near-critical and post-critical reflections. The value of argument $k_P r^*_{PP}(x_n)$ at minimal frequency 3 Hz varies from 14 at zero offset to 38 at offset 2500 m. The value of this argument at maximal frequency 60 Hz varies from 299 at zero offset to 779 at offset 2500 m. The value of this argument at dominant frequency of 39 Hz changes from 188 to 490 at zero and maximum offsets, respectively.

Figure 17 presents the band-limited AVO data and its ERC-based and PWRC-based theoretical descriptions. The behavior of the AVO data is more complex than that for Model 1. The first maximum in the AVO data is associated with the PPP-type head wave arrival, while the second maximum corresponds to the PSP-type head wave. Despite the complexity of the AVO data, the ERC-based theoretical description exhibits a good fit to the AVO data, while the PWRC-based description substantially deviates from it.

Figure 18a and 18b shows the results of the four-parameter band-limited ERC-based and PWRC-based AVO inversions. The results generally resemble those obtained for Model 1 (Figure 14b), but the overall accuracy is almost twice as high. We suspect this is explained by the presence of an additional critical point which increases the sensitivity of the theoretical description to all the parameters. The PWRC-based AVO inversion produces relatively poor results for the offsets below the second critical point and almost constant errors behind the second critical point. While the accuracy of the estimated V_{S2} increases considerably, V_{S1} is still undefined.

DISCUSSION

We show that the ERC-based AVO inversion greatly improves the accuracy of estimated parameters as compared to the PWRC-based AVO inversion. The improvement is especially apparent when the near-critical and post-critical offsets come into play. This is explained by the wavefront curvature effect, which is captured by the ERC and ignored by the PWRC. We show also that incorporation of several frequencies rather than one enhances the accuracy of the ERC-based AVO inversion.

Although a significant improvement is observed when switching from the PWRC-based AVO inversion to the ERC-based AVO inversion, the computational effort is greater. The ERC-based AVO inversion, in particular the band-limited version of it, is CPU-demanding. The computational cost of band-limited AVO inversion

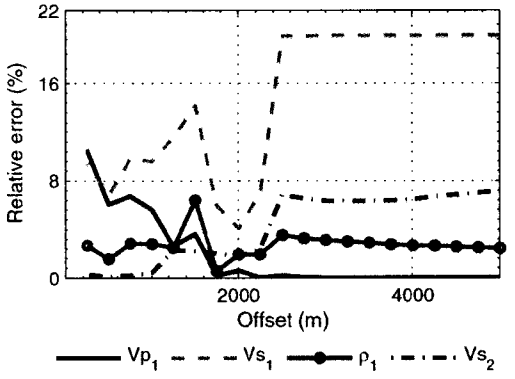

Figure 16. Relative error in the inversion results for the band-limited ERC-based AVO inversion of the Z-component AVO data.

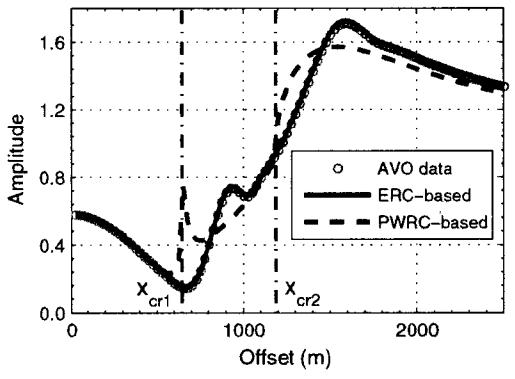

Figure 17. Band-limited AVO data for Model 2 and the corresponding theoretical descriptions calculated for the true model parameters.

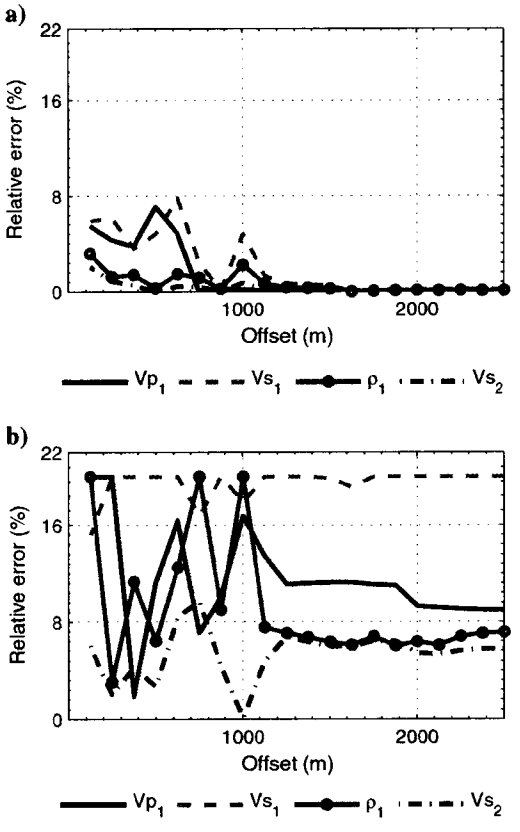

Figure 18. Relative error in the four-parameter AVO inversion as function of the offset range for Model 2. (a) ERC-based band-limited AVO inversion; (b) PWRC-based band-limited AVO inversion.

is 15 times higher than single-frequency AVO inversion, and it exhibits a nonlinear dependency on the number of frequencies involved in the inversion. There is therefore a trade-off between the desired quality of the inversion and its computational cost.

The proposed approach and a conventional way of performing AVO inversion in the industry are essentially different. A typical setup for an inversion implies the application of a weak-contrast plane-wave reflection coefficient, which is written in terms of the contrasts in elastic parameters. Such an inversion will therefore estimate the contrasts in the parameters across the reflecting interface. We incorporate post-critical offsets and strong parameter contrasts across the interface. ERCs cannot be easily linearized in a similar way as PWRCs. Our inversion therefore performs a somewhat broader task of estimating the absolute values of seismic parameters. We show that ERCs provide the possibility of defining five absolute parameters, while PWRCs are capable of estimating only four parameters.

In our tests, we recovered parameters both in the overburden and the underburden, by assuming two parameters in the underburden to be known. In principle, the ERC-based inversion allows retrieval of five parameters. However, one needs to carefully choose the estimated parameters, because the objective function may not be equally sensitive to all the parameters, at least for some offset ranges. The inversion does not in general allow recovering of the densities independently. Nevertheless, we can recover the full set of seismic parameters in the underburden if the density in the overburden is known. It is also natural to perform a combination of a traveltime inversion and an AVO inversion to improve the quality of parameter estimation above and below the target interface. The only information we may miss is the density estimate in the overburden.

We have shown examples of inverting multicomponent as well as single-component synthetic data. We realize that multicomponent data may not be available in the real-world tasks. However, we like to illustrate the difference in the performance of the inversion workflow for both cases. As we show in our examples, the quality of the inversion generally increases when we reconstruct the displacement along the ray. The comparison of 1C ERC-based AVO inversion with the multicomponent PWRC-based inversion shows that the former is still better than the latter.

Given that in marine surveys we obtain scalar omnidirectional pressure field, AVO data and its theoretical descriptions obey equations 11 and 15. We thus expect the inversion results to perform as well as in case of a multicomponent inversion.

Our numerical tests are performed for one plane interface, although the theory of ERCs can be extended for curved reflectors and layered overburden. We concentrated on the simplest model of one plane interface between two homogeneous half-spaces to demonstrate that ERCs help to significantly enhance the inversion performance. The initial results provide motivation for further studies.

We have also avoided the topic of irregular noise in the data, although some noise is brought in because of the numerical errors of the modeling algorithm in the pre-critical domain. Systematic noise, such as residual multiples, water-column noise, and ground-roll, which might tune with the data at the post-critical offsets (Landrø and Tsvankin, 2007), deserve an additional study.

Last, but not least, is the issue of quality of data processing prior to performing the inversion. There are particular requirements imposed on the processing sequence to condition the data for AVO inversion. One of the steps in such a sequence oftentimes is true amplitude imaging, which aims to remove the effects of wave propagation through the overburden to obtain the true reflection amplitudes at the target interfaces. The data after imaging become more regular with a better S/N ratio. However, the existing imaging algorithms assume that the interface is located in the far-field, and do not account for the reflections near and beyond the critical angle. In order to apply the ERC-based AVO inversion directly to imaged data, we need more advanced imaging techniques, which account for the wave phenomena associated with the critical angle. If the migration algorithm could properly account for post-critical reflections, we could directly exploit ERCs defined at the interface. At the current stage, we limit our work to nonimaged data. This issue needs a further investigation.

CONCLUSIONS

We show that long-offset data can significantly improve the performance of AVO inversion. It is, however, not enough to just increase the offset range. An adequate theoretical description of the observed AVO data is crucial for recovering the seismic parameters at long offsets. We propose to use the ERC instead of the PWRC. The ERC correctly describes the reflection of waves generated by point source at all offsets.

The synthetic tests show that including the near-critical and post-critical offsets in the AVO inversion based on PWRCs does not improve its quality and decreases the accuracy of S-wave velocity estimates in certain circumstances. Long-offset ranges increase the accuracy of parameter estimates in the AVO inversion based on ERCs. We achieve an error level of approximately 1% when including a wide range of offsets.

One of the advantages of our approach is the ability to recover five parameters because of the presence of the additional dimensionless parameter $\frac{\alpha_0 r_{pp}^*(0)}{V_{P1}}$. Although the quality of the five-parameter AVO inversion is somewhat lower than the quality of the four-parameter inversion, it still recovers the desired parameters with a high accuracy at the post-critical offsets.

Among the considered versions of the AVO inversion based on ERCs, we found the band-limited inversion to perform the best. The single-frequency AVO inversion produces, on average, less accurate results.

ACKNOWLEDGMENTS

Lyubov Skopintseva acknowledges Statoil ASA for financing her Ph.D. study at NTNU. We acknowledge Statoil ASA and the Russian Foundation for Basic Research (grant 07-05-00671) for support of this work and the Norwegian Research Council for financial support of the ROSE project at NTNU. We are grateful to the reviewers for constructive suggestions that helped us to greatly improve the paper.

APPENDIX A

REFLECTED PP-WAVEFIELD AT THE RECEIVER IN TERMS OF ERC

To theoretically describe the AVO data, we need to establish a link between the reflected wavefield and the ERC. There are three approaches to the description of the wavefields reflected from plane interfaces between two homogeneous media (Červený and Ravindra, 1971); a numerical representation, a local high-frequency

asymptotic description, and a rigorous plane-wave decomposition. The numerical representation is irrelevant for us since we seek an analytical form of the solution. The high-frequency asymptotic solution represents the reflected wave and the head wave around the critical ray using the Weber-Hermite functions. This approximation does not describe the interference between the two waves at the near-critical and post-critical offsets, and does not therefore fit our purpose. We use the rigorous plane-wave decomposition and exploit the results of Ayzenberg et al. (2009) to introduce the reflected wavefield at the receiver in terms of ERCs. We consider a model with two homogeneous half-spaces separated by a horizontal plane interface.

The interface is given by equation $x_3(x_1, x_2) = -h$ in the global Cartesian system. We assume for simplicity that the source is located at the origin (0, 0, 0), the receiver is placed on the same side of the interface as the source, and it has coordinates $\mathrm{x} = (x_1, x_2, x_3)$.

The reflected P-wavefield at the receiver can be represented by the Kirchhoff propagation integral

$$\mathbf{u}_{PP}(\mathrm{x}, \omega) = \int\int_S \mathbf{P}_P(\mathrm{x}, \mathrm{s}, \omega)\mathbf{u}_{PP}(\mathrm{s}, \omega)\mathrm{ds} \qquad \text{(A-1)}$$

where the reflected P-wavefield at the interface is represented by the convolutional reflection integral

$$\mathbf{u}_{PP}(\mathrm{s}, \omega) = \frac{1}{2\pi}\int\int_{S'} R_{PP}(\mathrm{s} - \mathrm{s}', \omega)\mathbf{u}_P^*(s', \omega)\mathrm{ds}' = \frac{1}{2\pi}\int\int_{S'} R_{PP}(\mathrm{s}', \omega)\mathbf{u}_P^*(\mathrm{s} - \mathrm{s}', \omega)\mathrm{ds}', \qquad \text{(A-2)}$$

$\mathbf{u}_P^*(\mathrm{s}', \omega) = \mathbf{H}_{PP}(\mathrm{s}', \tilde{\mathrm{s}}, \omega)\mathbf{u}_P(\tilde{\mathrm{s}}, \omega)$; $\mathbf{H}_{PP}(\mathrm{s}', \tilde{\mathrm{s}}, \omega)$ is a matrix operator which transforms the polarization vector $\mathbf{e}_P(\tilde{\mathrm{s}})$ at point $\tilde{\mathrm{s}}$ to polarization vector $\mathbf{e}_{PP}(\mathrm{s}')$ at point s'; $\mathbf{u}_P(\tilde{\mathrm{s}}, \omega)$ is the incident P-wavefield at point $\tilde{\mathrm{s}}$ of the interface; s' is a point in the Fresnel zone;

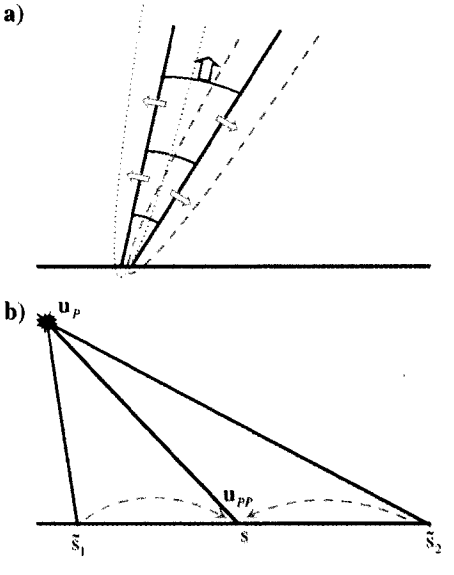

Figure A-1. Scheme of (a) propagation and (b) reflection of the wave generated by a point source.

$\mathbf{P}_P(\mathrm{x}, \mathrm{s}, \omega)$ is the propagation operator, $R_{PP}(\mathrm{s}', \omega)$ is the reflection operator, $d\mathrm{s} = d\mathrm{s}_1 d\mathrm{s}_2$, $d\mathrm{s}' = d\mathrm{s}_1' d\mathrm{s}_2'$. Wavefield $\mathbf{u}_P^*(\mathrm{s}', \omega)$ can be considered as the incident wave generated by the apparent source, which is a mirror image of the actual source with respect to the interface. The apparent source has coordinates $(0, 0, -2h)$. The wavefield generated by the apparent source differs from actual incident wavefield only by the polarization vector that coincides with the polarization vector of the reflected wave.

The wave propagation process described by equation A-1 is sketched in Figure A-1a. There are two different mechanisms for energy propagation; the propagation along the ray tube, which has been discussed in detail in ray theory (Červený, 2001) and the energy diffusion across the ray tube (Klem-Musatov et al., 2008). Figure A-1b illustrates reflection given by equation A-2. The operator decomposes the incident wavefield to plane waves at every point $\tilde{\mathrm{s}}$ of the interface, rotates the polarization vector with respect to the interface normal, multiplies each plane-wave with the corresponding PWRC, and then sums the obtained values at point s of the interface. The reflected field obtained at point s includes the contributions from all points $\tilde{\mathrm{s}}$.

Substituting equation A-1 to A-2, we obtain the four fold integral:

$$\mathbf{u}_{PP}(\mathrm{x}, \omega) = \int\int_S \mathbf{P}_P(\mathrm{x}, \mathrm{s}, \omega)\left\{\frac{1}{2\pi}\int\int_{S'} R_{PP}(\mathrm{s}', \omega)\mathbf{u}_P^*(\mathrm{s} - \mathrm{s}', \omega)\mathrm{ds}'\right\}\mathrm{ds} \qquad \text{(A-3)}$$

The integral in A-3 can be evaluated in the seismic frequency range using ERCs (Ayzenberg et al., 2009). We rearrange the integrals in A-3 to show this. It is known that for plane interfaces the following is valid: $\mathbf{P}_P(\mathrm{x}, \mathrm{s}, \omega) = \mathbf{P}_P(\mathrm{x} - \mathrm{s}', \mathrm{s}, \omega)$. We thus obtain:

$$\mathbf{u}_{PP}(\mathrm{x}, \omega) = \frac{1}{2\pi}\int\int_{S'} R_{PP}(\mathrm{s}', \omega)\mathbf{u}_P^*(\mathrm{x} - \mathrm{s}', \omega)\mathrm{ds}' \qquad \text{(A-4)}$$

where the vector integrand is represented by the propagation integral

$$\mathbf{u}_P^*(\mathrm{x} - s', \omega) = \int\int_S \mathbf{P}_P(\mathrm{x} - \mathrm{s}', \mathrm{s}, \omega)\mathbf{u}_P^*(\mathrm{s}, \omega)\mathrm{ds} = \int\int_S \mathbf{P}_P(\mathrm{x}, \mathrm{s}, \omega)\mathbf{u}_P^*(\mathrm{s} - \mathrm{s}', \omega)\mathrm{ds}. \qquad \text{(A-5)}$$

Exploiting the convolutional property for the reflection operator and defining the new variable $\mathrm{x}' = \mathrm{x} - \mathrm{s}'$, we obtain:

$$\mathbf{u}_{PP}(\mathrm{x}, \omega) = \frac{1}{2\pi}\int\int_{\tilde{X}'} R_{PP}(\mathrm{x} - \mathrm{x}', \omega)\mathbf{u}_P^*(\mathrm{x}', \omega)d\mathrm{x}', \qquad \text{(A-6)}$$

where x' represents a point in the Fresnel zone located at the observation surface.

Equation A-6 says that the reflected wavefield at the receiver is the convolution of the wavefield originating at the apparent source and evaluated at the receiver, and the reflection operator defined at the receiver.

Within the seismic frequency range, the spherical-wave $\mathbf{u}_P^*(\mathrm{x}', \omega)$ can be represented by the approximation:

$$\mathbf{u}_P^*(\mathrm{x}', \omega) \cong \frac{i}{V_{\mathrm{P1}}} S(\omega) \frac{e^{ik_P l(\mathrm{x}')}}{l(\mathrm{x}')} \mathbf{e}_{PP}(\mathrm{x}'), \qquad \text{(A-7)}$$

where $l(\mathrm{x}')$ is the distance between the apparent source and point x', $S(\omega)$ is the wavelet spectrum, k_P is the wavenumber, V_{P1} is the P-wave velocity in the overburden, $\mathbf{e}_{PP}(\mathrm{x}')$ is the polarization vector at the receiver.

Substituting equation A-7 to equation A-6 and applying the approach proposed by Ayzenberg et al. (2009), we obtain the reflected PP-wavefield in terms of ERCs:

$$\mathbf{u}_{PP}(\mathrm{x}, \omega) \cong \chi_{PP}[\mathrm{x}, \omega] \frac{i}{V_{\mathrm{P1}}} S(\omega) \frac{e^{ik_P l(\mathrm{x})}}{\sqrt{J_{PP}(\mathrm{x})}} \mathbf{e}_{PP}(\mathrm{x}) \qquad \text{(A-8)}$$

where $\chi_{PP}[\mathrm{x}, \omega] = \chi_{PP}[\theta(\mathrm{x}), k_P r_{PP}^*(\mathrm{x}), \mathbf{m}]$ is the ERC defined at the receiver, $r_{PP}^*(\mathrm{x})$ is the apparent wavefront radius at the receiver, $l(\mathrm{x})$ is the distance between the apparent source and the receiver, and $J_{PP}(\mathrm{x}) = [l(\mathrm{x})]^2$ is the geometrical spreading of the reflected PP-wave. Equation A-8 was heuristically obtained and tested on synthetic data modeled by the finite-difference method by Skopintseva et al. (2008, 2009). It represents a seismic frequency approximation, which is similar to high-frequency approximation, when the ERC is replaced by the PWRC. However, the ERC takes into account the interference between the reflected and the head waves in the near-critical and the post-critical domains. For homogeneous media with plane interfaces, we obtain: $l(\mathrm{x}) = l(\mathrm{s}) + l(\mathrm{x}, \mathrm{s})$, where $l(\mathrm{s})$ is the distance between the actual source and the reflection point, and $l(\mathrm{x}, \mathrm{s})$ is the distance between the reflection point and the receiver.

From the definition of ERCs in media with plane interfaces, we obtain that $r_{PP}^*(\mathrm{x}) = l(\mathrm{x})$. The ERC at the receiver is thus different from the one at the interface. The ERC at the interface is defined for reflection angle $\theta(\mathrm{s})$ and apparent radius $r_{PP}^*(\mathrm{s})$. The ERC at the receiver depends on reflection angle $\theta(\mathrm{x})$ and apparent radius $r_{PP}^*(\mathrm{x})$. The position of amplitude maximum and the oscillations at the post-critical offsets are different for the two ERCs. Indeed, when the reflected wavefield propagates from the interface to the receiver, the interference between the reflected wave and the head wave changes because of the different nature of their propagation. This causes the energy diffusion across ray tube during propagation (Figure A-1a). Quantity $r_{PP}^*(\mathrm{x})$ controls the diffusion. Representing the $r_{PP}^*(\mathrm{x})$ through $r_{PP}^*(\mathrm{s})$, we find the link between the two ERCs:

$$r_{PP}^*(\mathrm{x}) = r_P^*(\mathrm{s}) \left(1 + \frac{l(\mathrm{x}, \mathrm{s})}{l(\mathrm{s})}\right). \qquad \text{(A-9)}$$

REFERENCES

Aizenberg, A., M. Ayzenberg, H. B. Helle, and J. Pajchel, 2005, Reflection and transmission of acoustic wavefields at a curved interface of two inhomogeneous media: Continuum Dynamics, Acoustics of Inhomogeneous Media, **123**, 73–79.

Aki, K., and P. Richards, 2002, Quantitative Seismology (2nd ed.): University Science Books.

Ayzenberg, M., I. Tsvankin, A. Aizenberg, and B. Ursin, 2009, Effective reflection coefficients for curved interfaces in transversely isotropic media: Geophysics, **74**, no. 5, WB33–WB53, doi: 10.1190/1.3197862.

Ayzenberg, M. A., A. M. Aizenberg, H. B. Helle, K. D. Klem-Musatov, J. Pajchel, and B. Ursin, 2007, Three-dimensional diffraction modeling of singly scattered acoustic wavefields based on the combination of surface integral propagators and transmission operators: Geophysics, **72**, no. 5, SM19–SM34, doi: 10.1190/1.2757616.

Bluman, G. W., and S. Kumei, 1989, Symmetries and differential equations: Springer-Verlag.

Brekhovskikh, L. M., 1960, Waves in layered media: Academic Press.

Červený, V., 1961, The amplitude curves of reflected harmonic waves around the critical point: Studia Geophysica et Geodaetica, **5**, 319–351, doi: 10.1007/BF02585404.

Červený, V., 2001, Seismic Ray Theory: Cambridge University Press.

Červený, V., and R. Ravindra, 1971, Theory of Seismic Head Waves: University of Toronto Press.

De Santo, J. A., 1983, Scattering of scalar waves from a rough interface using a single integral equation: Wave Motion, **5**, 125–135, doi: 10.1016/0165-2125(83)90029-X.

Downton, J. E., and C. Ursenbach, 2006, Linearized amplitude variation with offset (AVO) inversion with supercritical angles: Geophysics, **71**, no. 5, E49–E55, doi: 10.1190/1.2227617.

Favretto-Cristini, N., P. Cristini, and E. de Bazelaire, 2009, What is a seismic reflector like?: Geophysics, **74**, no. 1, T13–T23, doi: 10.1190/1.3033216.

Himmelblau, D. M., 1972, Applied nonlinear programming: McGraw-Hill.

Kennett, B., 1984, Reflection operator methods for elastic waves: Wave Motion, **6**, 407–418, doi: 10.1016/0165-2125(84)90041-6.

Kennett, B. N., 1983, Seismic wave propagation in stratified media: Cambridge University Press.

Klem-Musatov, K., A. M. Aizenberg, J. Pajchel, and H. B. Helle, 2008, Edge and tip diffractions: Theory and applications in seismic prospecting: SEG.

Klem-Musatov, K. D., A. M. Aizenberg, H. B. Helle, and J. Pajchel, 2004, Reflection and transmission at curvilinear interface in terms of surface integrals: Wave Motion, **39**, 77–92, doi: 10.1016/j.wavemoti.2003.07.002.

Korn, G. A., and T. M. Korn, 1968, Mathematical handbook for scientists and engineers: Definitions, theorems, and formulas for reference and review: McGraw-Hill.

Kurt, H., 2007, Joint inversion of AVA data for elastic parameters by bootstrapping: Computers & Geosciences, **33**, 367–382, doi: 10.1016/j.cageo.2006.08.012.

Landrø, M., and I. Tsvankin, 2007, Seismic critical-angle reflectometry: A method to characterize azimuthal anisotropy?: Geophysics, **72**, no. 3 D41–D50. doi: 10.1190/1.2437145

Lavaud, B., N. Kabir, and G. Chavent, 1999, Pushing AVO inversion beyond linearized approximation: Journal of Seismic Exploration, **8**, 279–302.

Petrashen, G. I., 1957, Methods for the quantitative study of dynamics of seismic waves, Volume **1**: Leningrad University.

Riedel, M., and F. Theilen, 2001, AVO investigations of shallow marine sediments: Geophysical Prospecting, **49**, 198–212, doi: 10.1046/j.1365-2478.2001.00246.x.

Shuey, R. T., 1985, A simplification of the Zoeppritz equations: Geophysics, **50**, 609–614, doi: 10.1190/1.1441936.

Skopintseva, L. V., M. A. Ayzenberg, M. Landrø, T. V. Nefedkina, and A. M. Aizenberg, 2008, AVO inversion of long-offset synthetic PP data based on effective reflection coefficients: 70th EAGE Conference & Exhibition, Extended Abstracts, 609–614.

Skopintseva, L. V., M. A. Ayzenberg, M. Landrø, T. V. Nefedkina, and A. M. Aizenberg, 2009, Testing the performance of the AVO inversion based on effective reflection coefficients on long-offset synthetic PP-data: 71th EAGE Conference &Exhibition, Extended Abstracts, S022.

Skopintseva, L. V., T. V. Nefedkina, M. A. Ayzenberg, and A. M. Aizenberg, 2007, An approach to the AVO-inversion problem based on the effective reflection coefficients: 69th EAGE Conference & Exhibition, Extended Abstracts, P354.

Ursenbach, C. P., A. B. Haase, and J. E. Downton, 2007, An efficient method for AVO modeling of reflected spherical waves: Journal of Seismic Exploration, **16**, 561.

van der Baan, M., and D. Smit, 2006, Amplitude analysis of isotropic P-wave reflections: Geophysics, **71**, no. 6, C93–C103, doi: 10.1190/1.2335877.